Editors' Suggestion

Current Distribution on Capacitive Electrode-Electrolyte Interfaces

Zhijie Chen,[1,2,*] Lenya Ryzhik,[3] and Daniel Palanker[2,4]

[1] *Department of Electrical Engineering, Stanford University, Stanford, California 94305, USA*
[2] *Hansen Experimental Physics Laboratory, Stanford University, Stanford, California 94305, USA*
[3] *Department of Mathematics, Stanford University, Stanford, California 94305, USA*
[4] *Department of Ophthalmology, Stanford University, Stanford, California 94303, USA*

(Received 22 July 2019; revised manuscript received 22 November 2019; published 3 January 2020)

The distribution of electric current on an electrode surface in an electrolyte varies with time due to charge accumulation at a capacitive interface, as well as due to the electrode kinetics and concentration polarization in the medium. Initially, the potential at the electrode-electrolyte interface is uniform, resulting in a nonuniform current distribution due to the uneven ohmic drop of the potential in the medium. Over time, however, the nonuniform current density causes a spatially varying rate of the charge accumulation at the interface, breaking down its equipotentiality. We develop an analytical model to describe such a transition at a capacitive interface when the current is below the mass-transfer limitation and demonstrate that the steady distribution of the current is achieved when the current density is proportional to the capacitance per unit area, which leads to a linear voltage ramp at the electrode. More specific results regarding the dynamics of this transition are provided for a disk electrode, along with an experimental validation of the theoretical result. These findings may be of importance for many electrochemical applications and, in particular, for proper design of the electroneural interfaces.

DOI: 10.1103/PhysRevApplied.13.014004

I. INTRODUCTION

The dynamics of charge transfer across electrode-electrolyte interfaces is of great importance in electrochemistry in general and for many applications, including batteries, electroplating, electrolysis, chemical sensors and, in particular, bioelectronics. The distribution of current and voltage across such an interface is governed by multiple mechanisms, including the concentration polarization of the reactants in the medium, the kinetics of the electrode reactions, the ohmic drop in the bulk of the electrolyte, and charging of the electric double layer. The effects of the concentration polarization are modeled by the Warburg impedance, which is only significant at high current density, when the reactant concentration is considerably affected by the mass-transfer limitation [1,2]. The electrode kinetics is associated with faradaic electrochemical reactions and modeled by the charge-transfer resistance varying with voltage, which is considered linear at a lower current density according to the Butler-Volmer model [1,2]. The access resistance—the ohmic drop in the medium—is determined only by the electrode geometry and electrolyte conductivity. The electric double layer is modeled as a capacitance, where the Helmholtz plane in the electrolyte serves as the "plate" on the electrolyte side of this capacitive interface [3]. The double-layer capacitance is typically on the order of 10–20 $\mu F/cm^2$ for inert materials including carbon [4], platinum [5], and gold [6]. Additionally, some materials can exhibit a range of quasi-continuous oxidation states, enabling reversible storage of a much larger amount of charge than in a typical double-layer capacitance, and therefore known as pseudocapacitance [7–9]. Together, the double-layer capacitance and the pseudocapacitance are often called the supercapacitance [10].

Newman [11] calculated the primary current distribution at the interface of an equipotential (EP) disk electrode. It has been pointed out that both the electrode kinetics and the mass-transfer limitation result in secondary current distributions being more uniform than the primary one [12,13]. When the ohmic drop in the medium is the dominant part of the impedance, the calculation of the access resistance based on the EP boundary condition from Ref. [11] is broadly used [14–17]. The transient charge redistribution within the double layer on a disk electrode made of the same material has been described for controlled potential [18] and for controlled current [19], respectively. The frequency dispersion of such interfaces has been studied in Ref. [20].

However, there has been no theory describing the current distribution on electrodes of all geometries or with multiple surface materials. Such a theory is of interest in

*zcchen@stanford.edu

many electrochemical applications involving capacitive-coupling electrodes and especially for neural stimulation, where various geometries and materials are used in different applications. For neural-stimulation electrodes, the distribution of the electric current affects the stimulation thresholds and tissue safety and extra care should be taken to avoid irreversible electrochemical reactions. Therefore, materials of large charge storage capacity are often used to minimize the voltage swing and to ensure that the charge transfer is fully reversible, i.e., pseudocapacitive.

In this study we demonstrate, for any electrode geometry, that in the absence of the concentration polarization, the steady-state current distribution is achieved when the current density is proportional to the surface capacitance per unit area (PCD), where the boundary condition is not necessarily EP and the electrode potential converges to a linear ramp. For an electrode made of the same material, PCD implies a uniform current density (UCD). Initially, current begins to flow at a nonuniform density from the EP surface, but over time the uneven charge accumulation at the Helmholtz plane, as well as that in the pseudocapacitance, begins to affect the voltage drop across the double layer. Such uneven potential at the Helmholtz plane rearranges the electric field in the electrolyte and hence redistributes the current density, until the system reaches the PCD steady state.

Note that we model the possibly changing equilibrium potential of the associated electrochemical reactions by the pseudocapacitance, while Refs. [18,19] assumed constant reaction potentials. Therefore, in their notion, the steady state was resistive and unrelated to the surface capacitance. More recent studies [3,21] have assumed ideally polarizable disk electrodes—with no faradaic reactions—and have described the transition from the primary current distribution to the steady state using finite-element models, yielding only numerical solutions. However, without analytical description, fitting the numerical results to the *RC* approximations provides only a limited understanding of the transition, let alone that such finite-element models are usually intractable for an arbitrary electrode geometry. Nevertheless, the results have been widely adopted in practical applications [22–25].

The general model in this paper presents the transition from the initial current distribution to PCD for any electrode geometry and material composition, while considering the effects of the supercapacitance, the electrode kinetics, and the ohmic drop. We develop a framework to study capacitive interfaces with sinusoidal waveforms, chronoamperometry (controlled potential), or chronopotentiometry (controlled current), using the bra-ket notation. We demonstrate the application of this framework to a disk electrode, which agrees with the previous analytical results. We also demonstrate validation of some of these results experimentally.

II. THE SYSTEM MODEL

Typically, an equivalent-circuit model of the electrode-electrolyte interface with supercapacitance includes the double-layer capacitance C_d, the pseudocapacitance C_p, the faradaic leakage resistance R_f, the charge-transfer resistance $R_{\rm ct}$, the Warburg impedance Z_w, and the access resistance R_a [1,26], as shown in Fig. 1(a). The complex Warburg impedance has a constant angle of $-\pi/4$, which is a result of the phase delay between the current and the concentration polarization, stemming from the diffusion of reactants. It is a special case of a constant phase element (CPE). In more complicated models, more than one CPE may be included, the detailed mechanisms of which often remain unclear [27].

We are interested in the conditions in which the current density is below the mass-transfer limitation and hence Z_w is insignificant. The limiting current density is given by Eq. (28) of Ref. [12] for a disk electrode. We also assume negligible faradaic leakage. The charge transfer across the interface in this case is governed by the distributed capacitance and the charge-transfer resistance at the interface and by the ohmic drop in the medium. Thereby, our circuit can be simplified to that shown in Fig. 1(b). The model studied in Ref. [3] is a special case when $C_p = 0$ and the one in Refs. [18] and [19] is when $C_p \to +\infty$.

For an extended electrode, the capacitance, the charge-transfer resistance, and the access resistance are

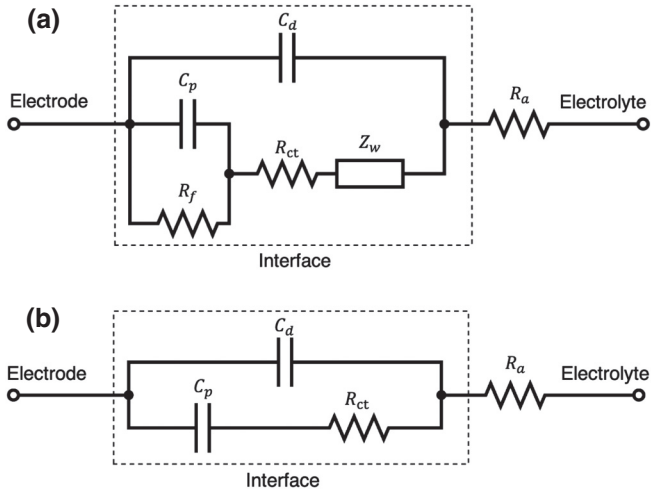

FIG. 1. Diagrams of the equivalent-circuit models of the electrode-electrolyte interface. The other electrodes of the electrochemical cell are omitted for simplicity. (a) A complete circuit model with pseudocapacitance includes the double-layer capacitor C_d, the pseudocapacitance C_p, the faradaic leakage resistance R_f, the charge-transfer resistance $R_{\rm ct}$, the Warburg resistance Z_w, and the access resistance R_a. (b) When the contributions to the total impedance from R_f and Z_w are negligible, the circuit model can be simplified. To model an ideally polarizable electrode, let $C_p = 0$.

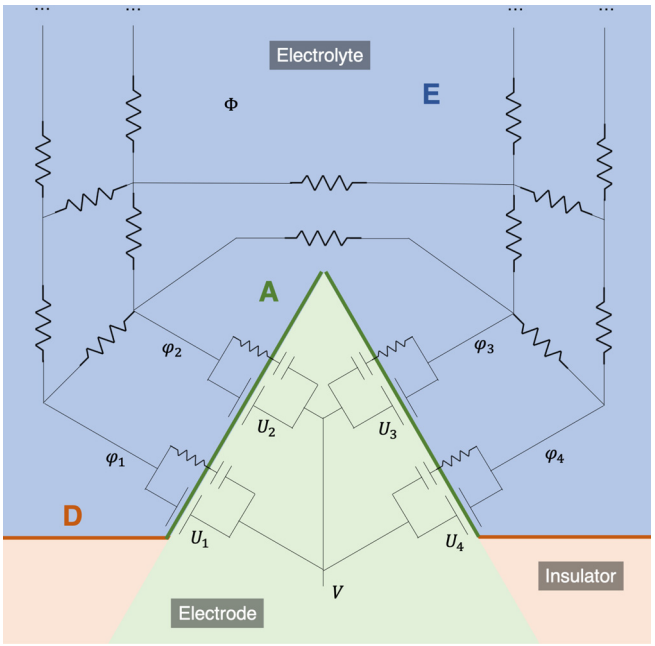

FIG. 2. A schematic illustration of the system, overlaid with the discretized version of the circuit diagram. The boundary of the electrolyte E consists of the insulating surface D and the electrode-electrolyte interface A. The electrode has the same potential V throughout its bulk but the potential drop U across the interface is generally a function of the location. Therefore, the potential in E just next to A is also a spatially varying function φ. Different locations at A have different access resistance to a return electrode at infinity.

distributed, as illustrated in Fig. 2. Each location on the interface is approximated by a discrete circuit in Fig. 1(b). Although illustrated with discrete components, our mathematical treatment makes no explicit discretization. Note that we only study half of the electrochemical cell, assuming that the current is collected on a large counter electrode infinitely far away.

In Fig. 2, E denotes the subset of the three-dimensional (3D) space occupied by the electrolyte. Its boundary with the electrode is denoted by A and has an insulating surface, denoted by D. $A \bigcup D = \partial E \subset E$. Let $\Phi(\mathbf{r}, t)$ denote the potential distribution in E as a function of both the spatial variable $\mathbf{r}$ and time t. We choose $\Phi(\infty) = 0$ and define φ as the two-dimensional restriction of Φ on A:

$$\varphi(\mathbf{r}, t) := \Phi(\mathbf{r}, t), \quad \mathbf{r} \in A. \tag{1}$$

The electrode is EP in its bulk, the potential of which as a function of time is denoted as $V(t)$. A nonuniform potential drop across the surface, which also varies with time, is denoted by $U(\mathbf{r}, t)$:

$$\varphi(\mathbf{r}, t) + U(\mathbf{r}, t) = V(t). \tag{2}$$

U is the voltage across C_d and we denote the potential drop across C_p by $U_p(\mathbf{r}, t)$. Let $C_p(\mathbf{r})$ and $C_d(\mathbf{r})$ be the pseudocapacitance and the double-layer capacitance per unit area on A, respectively. $R_{\rm ct}(\mathbf{r})$ is the charge-transfer resistance times the unit area on A. Typically,the pseudocapacitance is much larger than the double-layer capacitance [10]. For an area in which no electrochemical reactions take place, we may set $C_d = 0$, $R_{\rm ct} = 0$, and C_p the double-layer capacitance, so that $C_p(\mathbf{r}) \gg C_d(\mathbf{r})$ for $\forall \mathbf{r} \in A$.

In E, the current density is

$$\mathbf{i}(\mathbf{r}, t) := -\frac{1}{\rho}\nabla\Phi(\mathbf{r}, t), \tag{3}$$

where ρ is the resistivity of the electrolyte. On D, insulation implies zero normal current:

$$\mathbf{i}(\mathbf{r}) \cdot \mathbf{n}(\mathbf{r}) = 0, \quad \mathbf{r} \in D, \tag{4}$$

where the unitary $\mathbf{n}(\mathbf{r})$ is normal to the surface at $\mathbf{r}$ pointing to the electrolyte side. We choose the direction of $\mathbf{n}(\mathbf{r})$ as positive for current flow and define the normal current density on A:

$$i(\mathbf{r}, t) := \mathbf{i}(\mathbf{r}, t) \cdot \mathbf{n}(\mathbf{r}), \quad \mathbf{r} \in A. \tag{5}$$

Only the normal current component contributes to the charge accumulation on A. Conceptually, we may divide i into two components: the faradaic component i_a (the C_p–$R_{\rm ct}$ path) and i_b that charges the double layer (the C_d path). By definition,

$$i_a(\mathbf{r}, t) + i_b(\mathbf{r}, t) = i(\mathbf{r}, t). \tag{6}$$

i_a drives the voltage of the pseudocapacitance by

$$i_a(\mathbf{r}, t) = C_p(\mathbf{r})\dot{U}_p(\mathbf{r}, t), \tag{7}$$

and, similarly, for i_b we have

$$i_b(\mathbf{r}, t) = C_d(\mathbf{r})\dot{U}(\mathbf{r}, t). \tag{8}$$

The two current paths have the same potential drop:

$$R_{\rm ct}(\mathbf{r})i_a(\mathbf{r}, t) + U_p(\mathbf{r}, t) = U(\mathbf{r}, t). \tag{9}$$

The potential Φ satisfies the Laplace's equation:

$$\Delta\Phi = 0, \tag{10}$$

with the boundary conditions (1), (4), and $\Phi(\infty) \to 0$ as $\text{dist}(\mathbf{r}, A) \to +\infty$. Given the boundary condition φ, the potential Φ is fully determined and thus so is i. As Eq. (10) and all its boundary conditions are linear, there is a linear

mapping from φ to i, which we denote as a linear operator $\hat{\mathbf{S}}$:

$$\hat{\mathbf{S}}\varphi = i. \tag{11}$$

Because of the uniqueness of the electric field, $\hat{\mathbf{S}}$ is reversible. Define $\hat{\mathbf{R}}_a := \hat{\mathbf{S}}^{-1}$. Combine Eqs. (2), (6), (8), and (11), so that Eq. (6) gives

$$i_a = \hat{\mathbf{S}}\varphi - C_d(V' - \dot{\varphi}). \tag{12}$$

We take the derivative of Eq. (9) and use Eqs. (2) and (7):

$$R_{\rm ct}\dot{i}_a + C_p^{-1} i_a = V' - \dot{\varphi}. \tag{13}$$

Combine Eqs. (12) and (13):

$$\begin{aligned}\hat{\mathbf{R}}_a R_{\rm ct} C_p C_d \ddot{\varphi} + \left[\hat{\mathbf{R}}_a C_d + \left(\hat{\mathbf{R}}_a + R_{\rm ct}\right) C_p\right]\dot{\varphi} + \varphi \\ = \hat{\mathbf{R}}_a R_{\rm ct} C_p C_d V'' + \hat{\mathbf{R}}_a (C_d + C_p) V'.\end{aligned} \tag{14}$$

At the steady state of current distribution, by Eq. (11), φ no longer changes with time:

$$\ddot{\varphi} = \dot{\varphi} = 0. \tag{15}$$

Thus at steady state we have

$$i(\mathbf{r}) = \hat{\mathbf{S}}\varphi = R_{\rm ct} C_p C_d V''(t) + (C_d + C_p) V'(t). \tag{16}$$

In Eq. (16), the left-hand side is time independent, implying that there is a constant v so that

$$R_{\rm ct}\frac{C_p C_d}{C_d + C_p} V'' + V' = v. \tag{17}$$

Therefore, V' converges to v with time constant $R_{\rm ct} C_p C_d/(C_d + C_p)$, which may vary in space. The "steady" steady state has $V'' = 0$ and yields

$$i(\mathbf{r}) = \left[C_d(\mathbf{r}) + C_p(\mathbf{r})\right] v. \tag{18}$$

Because v is constant in space, at steady state the (normal) current density on the electrode surface is proportional to the capacitance per unit area. Note that a capacitive interface requires $v \neq 0$ for nonzero steady states of current distribution.

By Eq. (14), the characteristic polynomial of the system is

$$p(x) = x^2 \hat{\mathbf{R}}_a R_{\rm ct} C_p C_d + x\left[\hat{\mathbf{R}}_a C_d + \left(\hat{\mathbf{R}}_a + R_{\rm ct}\right) C_p\right] + \hat{\mathbf{I}}, \tag{19}$$

where $\hat{\mathbf{I}}$ is the identity operator. As proven in Appendix A, the operator $\hat{\mathbf{S}}$ is positive definite and so is $\hat{\mathbf{R}}_a$. $R_{\rm ct}$ and C_d are positive functions. Since $C_p \gg C_d$, the coefficient of the first-order term of Eq. (19) is dominated by C_p. Therefore, we may perturb the term $\hat{\mathbf{R}}_a C_d$ by its magnitude to make the system more tractable. We define a perturbation operator

$$\hat{\mathbf{P}} := -\hat{\mathbf{R}}_a\left(\hat{\mathbf{R}}_a + R_{\rm ct}\right)^{-1}, \tag{20}$$

the operator norm of which is bounded by 1. We perturb $p(x)$:

$$p(x) \approx \tilde{p}(x) := p(x) + x\hat{\mathbf{R}}_a C_d \hat{\mathbf{P}}. \tag{21}$$

Let $\hat{\mathbf{T}}_a = \left(\hat{\mathbf{R}}_a + R_{\rm ct}\right) C_p$, and $\hat{\mathbf{T}}_b = \hat{\mathbf{R}}_a R_{\rm ct} C_d\left(\hat{\mathbf{R}}_a + R_{\rm ct}\right)^{-1}$. We have

$$\tilde{p}(x) = \left(x\hat{\mathbf{T}}_b + \hat{\mathbf{I}}\right)\left(x\hat{\mathbf{T}}_a + \hat{\mathbf{I}}\right). \tag{22}$$

From Eq. (22), we know that the system has two sets of characteristic times, $\{\tau_a\}$ and $\{\tau_b\}$, corresponding to the eigenvalues of $\hat{\mathbf{T}}_a$ and $\hat{\mathbf{T}}_b$, respectively. Let $\{\Upsilon_a\}$ and $\{\Upsilon_b\}$ be the normalized (dimensionless) eigenfunctions of $\hat{\mathbf{T}}_a$ and $\hat{\mathbf{T}}_b^{\dagger}$, respectively. Each of the eigenfunctions corresponds to a eigenmode of φ, which is a potential distribution on A that elicits a current such that φ changes proportionally to itself. As mentioned, $\hat{\mathbf{R}}_a$ is positive definite, so $\{\tau_a\}$ and $\{\tau_b\}$ are positive. Furthermore, if the surface is uniform, namely $R_{\rm ct}$, C_p and C_d are constant, $\hat{\mathbf{T}}_a$ and $\hat{\mathbf{T}}_b$ are positive definite, and thus the eigenmodes are orthogonal within each set. Because $C_p \gg C_d$, $\{\tau_a\}$ are much larger than $\{\tau_b\}$. Thus, $\max\{\tau_a\}$ is the dominant time constant and $\{\varphi_b\}$ decay much faster than $\{\varphi_a\}$. Different eigenmodes of the same operator have different time constants because of the shape of the eigenmodes. Intuitively, if a eigenmode oscillates more rapidly in space, more charge transfers across small distances, having lower resistance and hence happening faster. $\hat{\mathbf{T}}_a$ may also have very small eigenvalues close to 0 but the magnitudes of the corresponding eigenmodes are very small as well. This is because the eigenmodes, which rapidly oscillate in space, usually do not correlate with the shape of the total potential distribution. We will show an example of this in Sec. IV.

III. RESPONSES TO TYPICAL STIMULI

With the model developed in Sec. II, we study the system responses to three typical stimuli in electrochemical measurements: sinusoidal waveforms in Sec. III A, chronoamperometry (controlled potential method) in Sec. III B, and chronopotentiometry (controlled current

method) in Sec. III C. With the approximation of Eq. (21), Eq. (14) becomes

$$\left(\hat{\mathbf{T}}_b\partial_t+\hat{\mathbf{I}}\right)\left(\hat{\mathbf{T}}_a\partial_t+\hat{\mathbf{I}}\right)\varphi = \left[\left(\hat{\mathbf{T}}_b\partial_t+\hat{\mathbf{I}}\right)\left(\hat{\mathbf{T}}_a\partial_t+\hat{\mathbf{I}}\right)-R_{\rm ct}C_p\partial_t-\hat{\mathbf{I}}\right]V. \quad (23)$$

A. Sinusoidal waveforms

A sinusoidal waveform is applied to the electrode: $V(t)=V_0e^{j\omega t}$, where j is the imaginary unit. Use of the time-domain Fourier transform in Eq. (23) yields

$$\varphi=\left(j\omega\hat{\mathbf{T}}_a+\hat{\mathbf{I}}\right)^{-1}\left(j\omega\hat{\mathbf{T}}_b+\hat{\mathbf{I}}\right)^{-1} \times\left[-\omega^2\hat{\mathbf{T}}_b\hat{\mathbf{T}}_a+j\omega\hat{\mathbf{R}}_a(C_p+C_d)\right]V_0e^{j\omega t}. \quad (24)$$

It is not possible to solve Eq. (24) explicitly without assuming a specific electrode configuration but we can estimate the impedance,

$$\hat{\mathbf{Z}}=Vi^{-1}=\left[-\omega^2\hat{\mathbf{T}}_b\hat{\mathbf{T}}_a+j\omega\hat{\mathbf{R}}_a(C_p+C_d)\right]^{-1} \times\left(j\omega\hat{\mathbf{T}}_b+\hat{\mathbf{I}}\right)\left(j\omega\hat{\mathbf{T}}_a+\hat{\mathbf{I}}\right)\hat{\mathbf{R}}_a, \quad (25)$$

at the extremes of the frequency ω.

We now use $\|\cdot\|$ to denote the Hilbert-Schmidt norm. As explained in Sec. II, $\left\|\hat{\mathbf{T}}_a\right\|\gg\left\|\hat{\mathbf{T}}_b\right\|$. In order of magnitude, $\left\|\hat{\mathbf{R}}_a(C_p+C_d)\right\|$ is close to $\left\|\hat{\mathbf{T}}_a\right\|$.

When $\omega\left\|\hat{\mathbf{T}}_b\right\|\gg1$, $\hat{\mathbf{Z}}\approx\hat{\mathbf{R}}_a$ and we have

$$\varphi=V, \quad (26a)$$

$$i=\hat{\mathbf{S}}V. \quad (26b)$$

We see from Eq. (26a) that at high frequencies the interface is equipotential and from Eq. (26b) that the current is changing in phase with voltage and the access resistance associated with the EP boundary condition is measured.

When $\omega\left\|\hat{\mathbf{T}}_a\right\|\ll1$, $\hat{\mathbf{Z}}\approx\left[j\omega(C_p+C_d)\right]^{-1}$ and we have

$$\varphi=j\omega\hat{\mathbf{R}}_a(C_p+C_d)V, \quad (27a)$$

$$i=j\omega(C_p+C_d)V. \quad (27b)$$

We see from Eq. (27a) that at low frequencies, the interface is not equipotential and from Eq. (27b) that the current is shifted by 90° and is proportional to the total surface capacitance C_p+C_d.

Now, if $\omega\left\|\hat{\mathbf{T}}_a\right\|\gg1$ but $\omega\left\|\hat{\mathbf{T}}_b\right\|\ll1$, we have

$$\hat{\mathbf{Z}}\approx C_p^{-1}\hat{\mathbf{S}}\left(\hat{\mathbf{R}}_a+R_{\rm ct}\right)C_p\hat{\mathbf{R}}_a. \quad (28)$$

Equation (28) is more intuitive when $R_{\rm ct}$ and C_p are uniform, which gives $\hat{\mathbf{Z}}=\hat{\mathbf{R}}_a+R_{\rm ct}$. Similar to high frequencies, at middle frequencies, the boundary is equipotential and the current is in phase with the voltage. The impedance is the sum of the access resistance and the charge-transfer resistance.

B. Chronoamperometric response

To study the transient behavior, we focus on the eigenmodes with long characteristic times and assume that all eigenmodes of $\hat{\mathbf{T}}_b$ decay infinitely fast. Explicitly, we assume $\hat{\mathbf{T}}_b\partial_t+\hat{\mathbf{I}}\approx\hat{\mathbf{I}}$ and Eq. (23) becomes:

$$\hat{\mathbf{T}}_a\dot{\varphi}+\varphi=\hat{\mathbf{R}}_aC_p\dot{V}. \quad (29)$$

Without loss of generality, we assume that $U_p(\mathbf{r},0)=U(\mathbf{r},0)=0$, and $V(t)=0$ when $t\le0$. We take $V(t)$ of the form $V(t)=V_0+vt$ for $t>0$. Since $U_p(t)$ must be continuous, we have

$$\left(R_{\rm ct}+\hat{\mathbf{R}}_a\right)i(\mathbf{r},0^+)=V(0^+). \quad (30)$$

At steady state, we have $\dot{\varphi}=0$. Together, we have

$$\varphi(0^+,\mathbf{r})=\hat{\mathbf{R}}_ai(\mathbf{r},0)=\hat{\mathbf{R}}_a\left(R_{\rm ct}+\hat{\mathbf{R}}_a\right)^{-1}V_0, \quad (31a)$$

$$\varphi(\infty,\mathbf{r})=\hat{\mathbf{R}}_aC_p(\mathbf{r})v. \quad (31b)$$

Let $\Upsilon_{a,l}$ be the lth normalized eigenfunction of $\hat{\mathbf{T}}_a$, corresponding to the eigenvalue τ_l. We expand φ in the basis $\{\Upsilon_a\}$, with the coefficients $\{\varphi_l\}$. If C_p is uniform, $\{\Upsilon_a\}$ is orthonormal and the expansion is straightforward:

$$\varphi_l(t)=\langle\Upsilon_{a,l}(\mathbf{r})|\varphi(\mathbf{r},t)\rangle\,. \quad (32)$$

For the more general case when C_p is not uniform, we perform the Gram-Schmidt orthogonalization to $\{\Upsilon_a\}$ with a coefficient matrix $\mathbf{G}$:

$$\begin{bmatrix}\tilde{\Upsilon}_{a,1}\\ \tilde{\Upsilon}_{a,2}\\ \tilde{\Upsilon}_{a,3}\\ \vdots\end{bmatrix}=\mathbf{G}\begin{bmatrix}\Upsilon_{a,1}\\ \Upsilon_{a,2}\\ \Upsilon_{a,3}\\ \vdots\end{bmatrix}=\begin{bmatrix}1 & & & \\ g_{21} & g_{22} & & \\ g_{31} & g_{32} & g_{33} & \\ \cdots & \cdots & \cdots & \ddots\end{bmatrix}\begin{bmatrix}\Upsilon_{a,1}\\ \Upsilon_{a,2}\\ \Upsilon_{a,3}\\ \vdots\end{bmatrix}, \quad (33)$$

such that $\{\tilde{\Upsilon}_a\}$ is orthonormal. We have

$$\begin{bmatrix} \varphi_1 \\ \varphi_2 \\ \varphi_3 \\ \vdots \end{bmatrix} = \mathbf{G}^\intercal \begin{bmatrix} \langle \tilde{\Upsilon}_{a,1} | \varphi \rangle \\ \langle \tilde{\Upsilon}_{a,2} | \varphi \rangle \\ \langle \tilde{\Upsilon}_{a,3} | \varphi \rangle \\ \vdots \end{bmatrix}. \tag{34}$$

By the principle of superposition, we have

$$\begin{aligned} i(\mathbf{r}, t) &= \hat{\mathbf{S}} \varphi(\mathbf{r}, t) \\ &= C_p(\mathbf{r}) v + \hat{\mathbf{S}} \sum_l \left(\varphi_l(0) - \varphi_l(\infty) \right) \Upsilon_l(\mathbf{r}) e^{-t/\tau_l}. \end{aligned} \tag{35}$$

The solution consists of a steady-state component $C_p(\mathbf{r})v$, which is PCD, and a transient component consisting of eigenmodes $\{\varphi_l \Upsilon_l(\mathbf{r})\}$ that exponentially decay at the rates τ_l. We call such transient behavior the EP-PCD transition (or EP-UCD when the interface material is uniform), the longest characteristic time of which corresponds to the largest eigenvalue of $\hat{\mathbf{T}}_a$:

$$\tau_{\max} = \lambda_{\max} \left(\hat{\mathbf{T}}_a \right). \tag{36}$$

C. Chronopotentiometric response

With controlled total current, Eq. (29) still holds but the solution is not the superposition of exponentially decaying eigenmodes, since $\dot{V}$ is no longer constant in time. Without loss of generality, we assume that $U_p(\mathbf{r}, 0) = U(\mathbf{r}, 0) = 0$ and the total current $I_{\text{tot}}(t) = 0$ when $t \le 0$. We take $I_{\text{tot}}(t) = I_0$ for $t > 0$. Denote the current coefficient of the lth eigenmode by u_l:

$$u_l = \int_A \hat{\mathbf{S}} \Upsilon_{a,l} \, dS, \tag{37}$$

so that $\varphi_l u_l$ is the net current of $\varphi_l \Upsilon_{a,l}$. We expand $\hat{\mathbf{R}}_a C_p$ in basis $\{\Upsilon_a\}$ with coefficients $\{\upsilon_l\}$:

$$\begin{bmatrix} \upsilon_1 \\ \upsilon_2 \\ \upsilon_3 \\ \vdots \end{bmatrix} = \mathbf{G}^\intercal \begin{bmatrix} \langle \tilde{\Upsilon}_{a,1} | \hat{\mathbf{R}}_a C_p \rangle \\ \langle \tilde{\Upsilon}_{a,2} | \hat{\mathbf{R}}_a C_p \rangle \\ \langle \tilde{\Upsilon}_{a,3} | \hat{\mathbf{R}}_a C_p \rangle \\ \vdots \end{bmatrix}, \tag{38}$$

so that $\dot{V} \upsilon_l$ is the $\Upsilon_{a,l}$ component of $\hat{\mathbf{R}}_a C_p \dot{V}$.

For the initial and the steady-state conditions, Eqs. (30) and (31) still hold. We combine Eqs. (31a) and (34) and $V(0^+)$ is given by V_0 in

$$\begin{bmatrix} u_1 \\ u_2 \\ u_3 \\ \vdots \end{bmatrix}^\intercal \mathbf{G}^\intercal \begin{bmatrix} \langle \tilde{\Upsilon}_{a,1} | \hat{\mathbf{R}}_a \left(R_{\text{ct}} + \hat{\mathbf{R}}_a \right)^{-1} 1 \rangle \\ \langle \tilde{\Upsilon}_{a,2} | \hat{\mathbf{R}}_a \left(R_{\text{ct}} + \hat{\mathbf{R}}_a \right)^{-1} 1 \rangle \\ \langle \tilde{\Upsilon}_{a,3} | \hat{\mathbf{R}}_a \left(R_{\text{ct}} + \hat{\mathbf{R}}_a \right)^{-1} 1 \rangle \\ \vdots \end{bmatrix} V_0 = I_0. \tag{39}$$

We can thereby determine $\{\varphi_l(0^+)\}$.

The total current does not change, so we have

$$\sum_l \dot{\varphi}_l u_l = 0. \tag{40}$$

In basis $\{\Upsilon_a\}$, Eq. (29) becomes

$$\tau_l \dot{\varphi}_l \Upsilon_{a,l} + \varphi_l \Upsilon_{a,l} = \dot{V} \upsilon_l \Upsilon_{a,l}, \quad \forall l. \tag{41}$$

Let $\mathbf{y}$ be a vector of variables,

$$\mathbf{y}^\intercal = [V \;\; \varphi_1 \;\; \varphi_2 \;\; \varphi_3 \;\; \dots], \tag{42}$$

and let $\mathbf{\Gamma}$ be a matrix of coefficients,

$$\mathbf{\Gamma} = \begin{bmatrix} 0 & u_1 & u_2 & u_3 & \cdots \\ \upsilon_l & -\tau_1 & & & \\ \upsilon_2 & & -\tau_2 & & \\ \upsilon_3 & & & -\tau_3 & \\ \vdots & & & & \ddots \end{bmatrix}. \tag{43}$$

We combine Eqs. (40) and (41) and have

$$\Gamma \dot{\mathbf{y}} = \begin{bmatrix} 0 & \\ & \mathbf{I} \end{bmatrix} \mathbf{y}. \tag{44}$$

Γ has full rank and solving for the transient behavior with controlled current becomes a standard problem of a homogeneous linear dynamic system, as in Eq. (44).

IV. SOLUTION FOR A DISK ELECTRODE

We now consider a disk electrode placed at the center of an insulating plane, with electrolyte filling the half-space above the plane. For simplicity of mathematical forms, from here on we assume uniform surface material, with constant R_{ct}, C_p, and C_d. The majority of the theoretical derivation has been done in Ref. [18], with the assumption of a constant electrochemical reaction potential ($C_p \to \infty$). As a demonstration of our more intuitive framework developed in Secs. II and III B, we apply it to this problem in Sec. IV A, and then compare the results with experimental measurements in Sec. IV B.

A. Theoretical derivation

We consider a disk electrode of radius a. As defined in Sec. II, R_P, C_p, and C_d are uniform. In Cartesian coordinates, we have $E = \{(x, y, z \geq 0)\}$, $A = \{(x, y, 0) : \sqrt{x^2 + y^2} \leq a\}$, and $D = \{(x, y, 0) : \sqrt{x^2 + y^2} > a\}$. Following Ref. [11], we will use the elliptic coordinate system (ξ, η). The Laplace's equation in elliptic coordinates is

$$\Delta\Phi(\xi,\eta) = \partial_\xi\left[(1+\xi^2)\partial_\xi\Phi\right] + \partial_\eta\left[(1-\eta^2)\partial_\eta\Phi\right] = 0, \tag{45}$$

with the boundary conditions

$$\Phi(0,\eta) = \psi(\eta), \tag{46a}$$

$$\Phi(\infty,\eta) = 0, \tag{46b}$$

$$\frac{\partial}{\partial z}\Phi(\xi,0)\bigg|_{\xi>0} = 0. \tag{46c}$$

We note that

$$\partial_z|_{r\leq a, z=0} = \frac{1}{a\eta}\partial_\xi, \tag{47a}$$

$$\partial_z|_{r>a, z=0} = \frac{1}{a}\partial_\eta. \tag{47b}$$

By Ref. [12], the solution to Eq. (45) is

$$\Phi(\xi,\eta) = \sum_{l=0}^{\infty} k_l X_l(\xi) P_{2l}(\eta), \tag{48}$$

where $l \in \mathbb{N}$, k_l are constant coefficients, P_{2l} is the $2l$th Legendre polynomial of the first kind and $X_l(\xi)$ is the solution to

$$\left[(1+\xi^2)X'\right]' - 2l(2l+1)X = 0. \tag{49}$$

We normalize P_{2l}, so that $\tilde{P}_{2l} := \sqrt{4l+1}P_{2l}$ form an orthonormal basis of functions in $\{f \in C^\infty : [0,1] \to \mathbb{R}, f'(0) = 0\}$. k_l in Eq. (48) are chosen so that $\Phi(0,\eta)$ matches a given $\varphi(\eta)$. With $X_l(0) = 1$, Eq. (48) becomes

$$\Phi(\xi,\eta) = \sum_{l=0}^{\infty} |\tilde{P}_{2l}\rangle\, X_l(\xi)\, \langle\tilde{P}_{2l}|\varphi\rangle\,. \tag{50}$$

By the definition of $\hat{\mathbf{S}}$ in Eq. (11),

$$\hat{\mathbf{S}}\varphi(\eta) = i(\eta) = -\frac{1}{\rho}\partial_z\Phi(0,\eta)\bigg|_{r\leq a}. \tag{51}$$

By Eq. (47), we then have

$$\hat{\mathbf{S}} = -\frac{1}{\rho a\eta}\sum_{l=0}^{\infty} |\tilde{P}_{2l}\rangle\, X_l'(0)\, \langle\tilde{P}_{2l}|\,. \tag{52}$$

Equation [18] of Ref. [12] gives, without derivation, that

$$X_l'(0) = -\frac{2}{\pi}\left[\frac{(2l)!!}{(2l-1)!!}\right]^2. \tag{53}$$

A detailed derivation is provided in Sec. 6.9 of Ref. [28]. Appendix B provides the derivation in a more rigorous manner and proves the monotonicity of $X(\xi)$. Intuitively, this shows that potential distribution is monotonic along each hyperbolic line in the elliptic coordinates.

Therefore, the operator $\hat{\mathbf{S}}$ has the form

$$\hat{\mathbf{S}} = \frac{2}{\pi\rho a}\eta^{-1}\sum_{l=0}^{\infty} |\tilde{P}_{2l}\rangle\left[\frac{(2l)!!}{(2l-1)!!}\right]^2\langle\tilde{P}_{2l}|\,. \tag{54}$$

Since R_{ct} and C_p are uniform, we now use these two notations as scalars. $\hat{\mathbf{T}}_a$ becomes

$$\hat{\mathbf{T}}_a = C_p\left(\hat{\mathbf{S}}^{-1} + R_{\text{ct}}\hat{\mathbf{I}}\right), \tag{55}$$

which shares the same eigenspace with $\hat{\mathbf{S}}$. We define a dimensionless operator

$$\hat{\mathbf{A}} := \eta^{-1}\sum_{l=0}^{\infty} |\tilde{P}_{2l}\rangle\left[\frac{(2l)!!}{(2l-1)!!}\right]^2\langle\tilde{P}_{2l}|\,, \tag{56a}$$

so that $\hat{\mathbf{S}} = (2/\pi\rho a)\hat{\mathbf{A}}$. We have

$$\tau_a = \frac{\pi\rho a C_p}{2\lambda\left(\hat{\mathbf{A}}\right)} + R_{\text{ct}}C_p. \tag{57}$$

As $|\eta| \leq 1$, the smallest eigenvalue of $\hat{\mathbf{A}}$ can then be estimated as $\lambda_{\min}\left(\hat{\mathbf{A}}\right) \geq 1$ and

$$\max\{\tau_a\} \leq \left(\frac{\pi\rho a}{2} + R_{\text{ct}}\right)C_p. \tag{58}$$

The numerically computed first four eigenfunctions of $\hat{\mathbf{A}}$, together with their respective eigenvalues, are shown in Fig. 3. It turns out that the smallest eigenvalue of $\hat{\mathbf{A}}$ is about 1.8, which gives

$$\max\{\tau_a\} = (0.864\rho a + R_{\text{ct}})\,C_p. \tag{59}$$

Note the similarity between Φ and the electrostatic potential of a charged disk. Specifically, if a flat disk in free space has charge density $\sigma(r) = 2\varepsilon_0\rho i(r)$, then Φ is also the potential distribution around the charged disk. With UCD, the potential at the center of the disk electrode is

$$\varphi(r=0) = \int_0^a \frac{2\pi r \times 2\varepsilon_0\rho i}{4\pi\varepsilon_0 r}dr = \rho a i. \tag{60}$$

Although the access resistance is not well defined with UCD, since the electrode surface is not equipotential, we

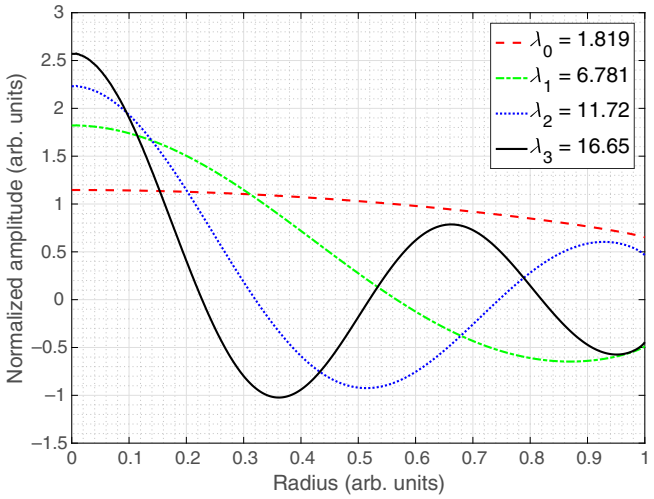

FIG. 3. The first four eigenfunctions and their respective eigenvalues of the operator $\hat{\mathbf{A}}$, in the cylindrical coordinate r. Each eigenfunction, which is also an eigenmode of $\hat{\mathbf{T}}_a$, evolves with a time constant determined by the corresponding eigenvalue of $\hat{\mathbf{T}}_a$. The smallest eigenvalue of $\hat{\mathbf{A}}$ is 1.819, corresponding to the largest time constant $(0.864\rho a + R_{\rm ct})\, C_p$, dominates the overall transition.

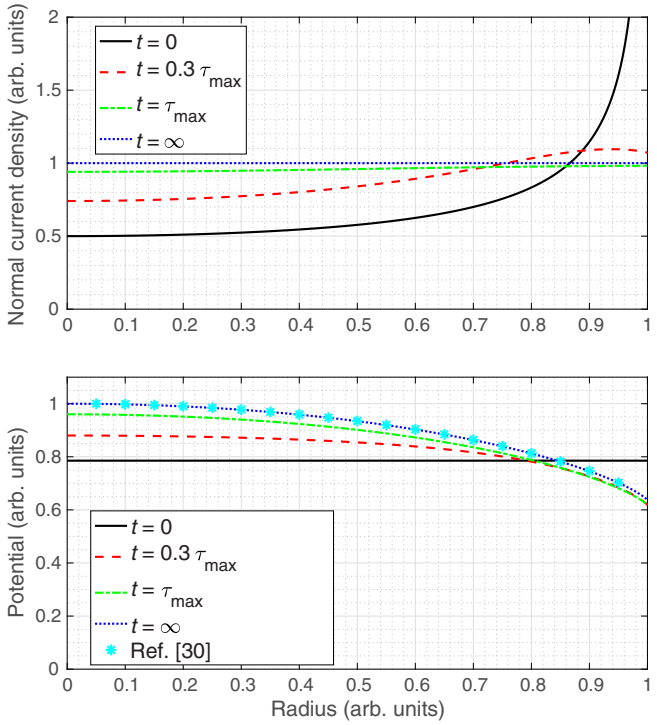

FIG. 4. Top panel: the current density on a disk electrode at four different time points. Here, $\tau_{\max}$ is the time constant of the slowest decaying eigenmode, $0.864\rho a C_p$. Bottom panel: the electric potential on a disk electrode at the same time points as in the top panel. The cyan asterisks are the analytical solution to the electrostatic potential of a uniformly charged disk given by Ref. [30], which is mathematically equivalent to the potential distribution under the UCD boundary condition.

can define an effective access resistance as the potential at the center of the electrode divided by the total current:

$$R_{a,\mathtt{eff}} = \frac{\rho a i}{\pi a^2 i} = \frac{\rho}{\pi a}. \tag{61}$$

This value is higher than the widely accepted access resistance value $\rho/(4a)$ of an equipotential disk electrode [11]. There are different definitions of the effective access resistance. For example, [29] defines $R_{a,\mathtt{eff}}$ as the average of φ divided by the total current. We choose our definition because the center of the electrode surface is the most typical point to sample when measuring potential in the electrolyte.

To illustrate the dynamics of the current redistribution in chronoamperometry, let ρ and vC_p, defined in Sec. III B, as well as the radius a, be unitary and let $R_{\rm ct} = 0$. To keep the total current the same at the initial state and at the steady state, we will choose $V_0 = \pi\rho\eta Ca/4$. The resulting evolution of the current density and the potential distribution on a disk electrode over time are shown in Fig. 4 and also as a video in the Supplemental Material [31].

B. Experimental validation

To experimentally verify whether the dynamics of the total current on a capacitive electrode-electrolyte interface matches the solution described by Eq. (35), we perform chronoamperometric measurements. From here on, all potentials are referred to the Ag-AgCl electrode, unless noted otherwise. In order to sustain higher current within the relatively small voltage window, we use an electrode coated with a sputtered iridium oxide film (SIROF)—a material known for its large charge-injection capacity (CIC) [32]. The continuous iridium valency of SIROF between 0 and 0.8 V [33], together with its porous surface [34], enables a large capacitance.

We use an electrochemical cell of the three-electrode configuration. The working electrode is an 80-μm-diameter platinum disk coated with 400 nm of SIROF. The electrode is treated with 4% NaClO solution and plasma cleaning, following the protocol of Ref. [35] (Secs. 2.15 and 3.3). A large (>1 cm^2) platinum grid is used as the counter electrode. The reference is an Ag-AgCl electrode in 3M KCl solution. The electrolyte is six-time-diluted phosphate-buffered saline (PBS) solution, the resistivity of which is 353 Ω cm, measured with an electrical-conductivity meter.

First, we validate that the electrode kinetics are invariant within the potential range and that concentration polarization is not the dominating factor in the electrode impedance. As shown in Fig. 5, the black solid line in the top panel represents a voltage step. The corresponding total current is shown by the black solid line of the

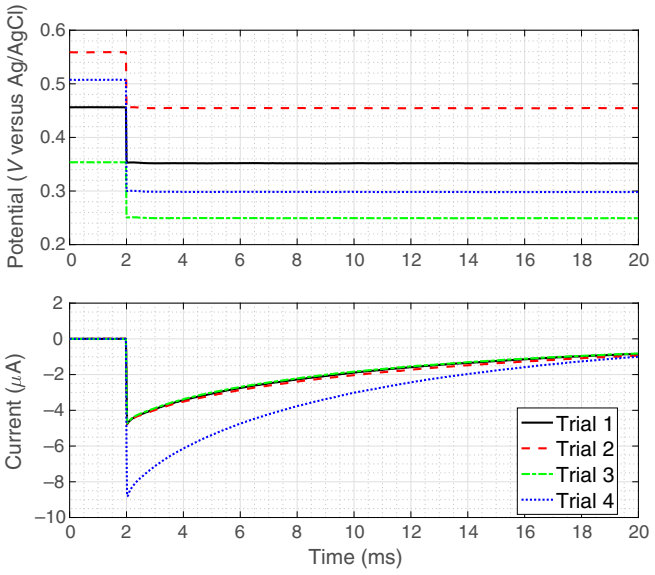

FIG. 5. Validation that the electrode kinetics is invariant within the potential range and that the concentration polarization is negligible at the selected settings. A curve in the top panel and the curve of the same style in the bottom panel represent the voltage and current measured, respectively. Trial 1 is the baseline. Trials 2 and 3 show that the electrode kinetics is varying with the potential, while trial 4 shows linear scaling with the amplitude of the voltage step, indicating that the concentration polarization has no effect on the circuit.

bottom panel (trial 1). To show that the electrode kinetics is not varying with potential, we offset the voltage pulse up and down by 100 mV (trials 2 and 3) and observe that the current does not change. To check whether the concentration polarization affects the current amplitude, we scale the voltage pulse by a factor of 2. The current nearly doubles as well, indicating that the concentration polarization is negligible, since the concentration overpotential does not scale linearly with the current density.

We observe very small charge-transfer resistance on this electrode, which allows us to neglect the effect of $R_{\rm ct}$ and combine C_p and C_d into one supercapacitance, C_s. To confirm this, we perform electrochemical impedance spectroscopy (EIS) and use the Levenberg-Marquardt method to fit the Bode plot to the circuit diagram in Fig. 6(a). The measurement and the fitting curves are plotted in Fig. 6(b). From the fitting, $R_{\rm ct} + R_a = 22.3\,{\rm k}\Omega$, within the 2% error range of the EP access resistance predicted by $\rho/(4a) = 22.0\,{\rm k}\Omega$. Per the discussion in Sec. III A, we confirm that $R_{\rm ct}$ is negligible. We also find that $C_s = 8.52\,{\rm mF/cm^2}$ from the fitting.

A voltage waveform including a step and a ramp, with $V_0 = -100\,{\rm mV}$ and $v = -3.24\,{\rm V/s}$, as defined in Sec. III B, is applied to the SIROF electrode (top panel in Fig. 4). Note that this waveform is different from the one used in Fig. 4 and hence the total current at the initial

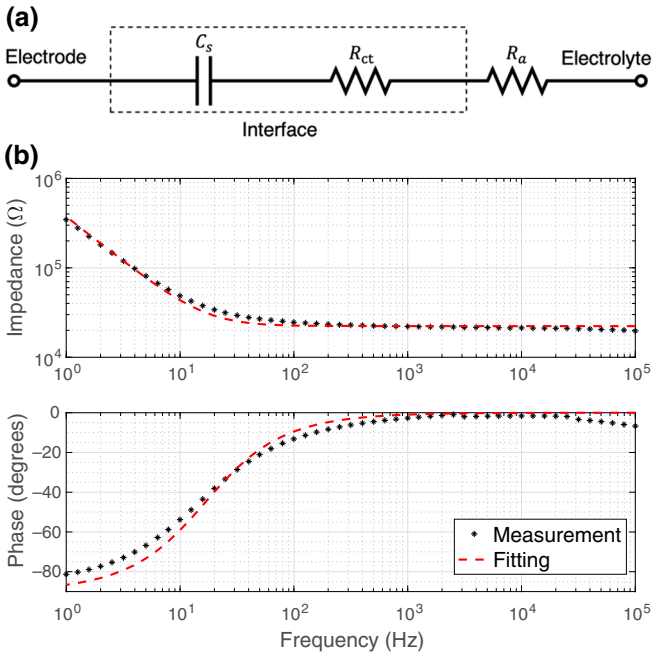

FIG. 6. (a) The circuit diagram of the fitting model. (b) The EIS Bode plot of the 80-μm-diameter SIROF disk electrode.

and the steady states is not the same either. The resulting current waveform is shown in the same panel.

One competing theory is that the surface instantly exchanges charge laterally, so the charge accumulation in the capacitor is uniform and the interface is always EP. This is the assumption behind the *RC* fitting in Refs. [3], [17], and [21]. To compare the experimental results with the predictions of the constant-EP theory and of the EP-UCD transition, the time derivative of the total current is calculated and plotted for both models and the measurement. The EP-UCD prediction is from Eq. (35), while the constant-EP prediction is a simple *RC* process. As can be seen in the bottom panel of Fig. 7, the measurement matches our theory rather than the constant-EP assumption.

V. DISCUSSION

A highly conductive electrode is always equipotential in its bulk but this equipotentiality is often confused with the surface layer of electrolyte at the interface, which is the boundary typically modeled as the Helmholtz plane. Electrode kinetics and concentration polarization are the two mechanisms previously considered to cause uniform secondary current distribution. Another important mechanism is the charge accumulation on the interface, which is often underappreciated in applications since it is not reflected in the initial current distribution. Previously, this effect has only been modeled for disk electrodes of uniform surfaces, assuming constant reaction potentials [18,19] or no electrochemical reactions [3,21].

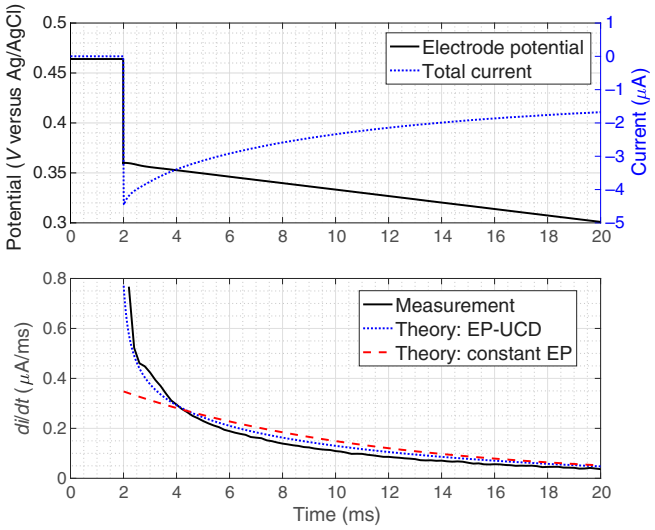

FIG. 7. Top panel: the voltage waveform applied to the SIROF electrode and the measured current. Bottom panel: the time derivative of the current from the measurement and the theoretical predictions calculated with two different theories: EP-UCD transition and constant EP.

As we show in Sec. II, for any geometry and any combination of surface materials, the current density eventually reaches the PCD steady state (or a UCD if the capacitance per unit area is the same over the whole electrode). Redistribution of the current from the initial nonuniform spread at an equipotential state is driven by the uneven charge accumulation at the capacitive interface until it reaches the PCD, when the potential of all parts of the interface rises at the same rate. This transition is described by the superposition of exponentially decaying eigenmodes, each of which has a different time constant. Each eigenmode is a surface potential distribution that elicits the circuit response to change itself proportionally. The shorter the time constant is, the faster the eigenmode decays. For a disk electrode of radius a and with uniform surface capacitance C, the dominant (longest) time constant is $0.864\rho Ca$, only 10% larger than the simple RC time constant $\tau_{\mathrm{EP}} = \pi\rho Ca/4 = 0.785\rho Ca$, where the EP access resistance $R_{\mathrm{EP}} = \rho/(4a)$ is assumed. In earlier finite-element modeling [3], the total current was fitted to one simple RC process, resulting in an 8.7% increment of the time constant compared to τ_{EP}, which roughly matches our result. Strictly speaking, there are two sets of eigenmodes and time constants, dominated by the pseudocapacitance C_p and the double-layer capacitance C_d, respectively. However, since the latter is faster than the former, when studying the transient behavior, we consider the latter to be instant, with a negligible effect on the circuit behavior. This requires $C_p \gg C_d$ everywhere, which may not be true if a surface consists of both electrochemically active parts and inert parts, but we can avoid this subtlety by choosing, nominally, $C_d = 0$, $R_{\mathrm{ct}} = 0$, and C_p, the double-layer capacitance. Empirically, the inverse time constants of different eigenmodes are separated almost evenly, which is equivalent to an asymptotic approximation conjectured by Troesch and Troesch [36] in a solution of a problem in fluid dynamics and confirmed computationally up to the 200th time constant [28].

It is important to note that the measurements of the access resistance using EIS correspond to the high end of the frequency range. At frequencies exceeding the inverse time constants of the current redistribution, the interface remains practically equipotential. Therefore, the access resistance measured in EIS is associated with the EP boundary condition. In the middle of the frequency range, we should see the sum of the EP access resistance and the charge transfer resistance, if C_p and C_d are separated sufficiently far apart.

Under the constant-EP boundary condition, the current in response to a voltage step with a ramp is a simple exponential decay to the steady state, with a RC time constant. Distinguishing this curve from a plot corresponding to our theory is not easy, since the dominant time constant is only slightly longer than in the constant-EP theory and the magnitude of the slowest eigenmode is the largest. Therefore, the bottom panel in Fig. 7 compares the time derivative of the total current. Since the constant-EP theory has only one decaying mode, while the EP-UCD transition has infinitely many and much faster decaying eigenmodes, the total current decreases faster at the beginning of the pulse, as can be seen in the plot.

At steady state, the PCD boundary condition enables control of the current distribution on various parts of the interface by selecting electrode materials of different capacitance per unit area. For example, if a part of the Au electrode is coated with SIROF and the pulse duration exceeds the characteristic EP-PCD transition time, the current will flow primarily through the SIROF area, while the Au surface will be practically passive, since its capacitance is about 1000 times smaller than that of SIROF. This effect was discovered in Ref. [37] but only analyzed using a discrete-circuit approximation. The phenomenon of PCD greatly simplifies the 3D electrode fabrication by electroplating: the side walls of the Au-electroplated electrode do not have to be coated with an insulator. They can remain exposed to the liquid since the SIROF on top of these walls will collect the vast majority of the current [38–40]. Similarly, the leads to high-capacitance electrodes—for example, the electrodes used in Ref. [41]—do not have to be well insulated from the medium as long as their capacitance is much smaller than that of the target electrode.

An understanding of the distribution of the electric field in the medium is particularly important for proper design of the electroneural interfaces. For example, if the pulse duration is significantly shorter than the EP-PCD transition time, the electric current will flow primarily from the

electrode edges. This will result in a highly enhanced electric field in these areas, which may stimulate and even damage the nearby cells much more than the average current density calculated by dividing the total current by the total electrode area [42]. The edge effect can be effectively avoided if the electrode capacitance is selected such that the characteristic transition time is below the intended pulse duration. In addition, the electrode capacitance can be gradually reduced toward the edges, for example, by decreasing the SIROF thickness using partial shadowing techniques.

VI. CONCLUSIONS

We provide an analytical solution describing the dynamics of the current redistribution on capacitive electrode-electrolyte interfaces and validate our theory experimentally. We demonstrate that the current and voltage redistribute over time from the initial nonuniform spread to the steady state, where the current density at the surface is proportional to the capacitance per unit area. This transition can be described as a superposition of the exponentially decaying eigenmodes. The slowest and dominant eigenmode of a disk electrode has a time constant similar to the *RC* time constant of the electrode. We also note that since the EIS-based measurements of the access resistance are performed at high frequencies, they correspond to an equipotential boundary condition, which is different from the access resistance at low frequencies. To avoid the strong edge effects on large electrodes, the capacitance of the electrode material should be selected so that the EP-PCD transition time does not significantly exceed the intended pulse duration.

ACKNOWLEDGMENTS

We would like to thank Professor Christopher Chidsey from Stanford University and Dr. Boshuo Wang from Duke University for the very helpful discussions. We would also like to thank Yibin Shu from the Institute of Education at Tsinghua University in China for his help with preparation of the key image. Funding was provided by the National Institutes of Health (Grants No. R01-EY-018608 and No. R01-EY-027786), the Stanford Neurosciences Institute, and Research to Prevent Blindness.

APPENDIX A

Here, we show that the operator $\hat{\mathbf{S}}$ defined in Eq. (11) is positive definite.

Proof. Let Φ and Ψ be two nonzero potential distributions in E and define

$$\phi_0(\mathbf{r}) := \Phi(\mathbf{r}), \quad \mathbf{r} \in A, \tag{A1a}$$

$$\phi_1(\mathbf{r}) := \Phi(\mathbf{r}), \quad \mathbf{r} \in D, \tag{A1b}$$

with similar definitions for ψ_0 and ψ_1. By Eqs. (4) and (5),

$$\nabla\Phi(\mathbf{r}) \cdot \mathbf{n}(\mathbf{r}) = 0, \quad \mathbf{r} \in D, \tag{A2a}$$

$$\nabla\Phi(\mathbf{r}) \cdot \mathbf{n}(\mathbf{r}) = -\rho\hat{\mathbf{S}}\phi_0, \quad \mathbf{r} \in A. \tag{A2b}$$

We may now write

$$\begin{aligned}\langle\psi_0, \hat{\mathbf{S}}\phi_0\rangle &= \int_A \psi_0\left(\hat{\mathbf{S}}\phi_0\right) dS \\ &= -\frac{1}{\rho}\int_A \Psi\nabla\Phi \cdot \mathbf{n}dS = -\frac{1}{\rho}\int_{A\bigcup D} \Psi\nabla\Phi \cdot \mathbf{n}dS.\end{aligned} \tag{A3}$$

The last equality above uses Eq. (A2a). By the divergence theorem and Eq. (10), we now have

$$\begin{aligned}-\int_{A\bigcup D} \Psi\nabla\Phi \cdot \mathbf{n}dS &= \int_E \nabla\left(\Psi\nabla\Phi\right) dV \\ &= \int_E \nabla\Psi \cdot \nabla\Phi dV + \int_E \Psi\Delta\Phi dV \\ &= \int_E \nabla\Psi \cdot \nabla\Phi dV;\end{aligned} \tag{A4}$$

thus

$$\langle\psi_0, \hat{\mathbf{S}}\phi_0\rangle = \frac{1}{\rho}\int_E \nabla\Psi \cdot \nabla\Phi dV. \tag{A5}$$

It follows that $\hat{\mathbf{S}}$ is Hermitian, which is the result of the Lorentz reciprocity. Furthermore, as

$$\int_E \|\nabla\Phi\|^2 dV > 0, \tag{A6}$$

we have

$$\langle\phi_0, \hat{\mathbf{S}}\phi_0\rangle > 0, \quad \forall\phi_0 \neq 0, \tag{A7}$$

and it follows that $\hat{\mathbf{S}}$ is positive definite.

APPENDIX B

The general solution to Eq. (49) is

$$X_l(\xi) = c_1 P_{2l}(j\xi) + c_2 Q_{2l}(j\xi), \tag{B1}$$

where $j = \sqrt{-1}$, $c_1, c_2 \in \mathbb{C}$ are coefficients and Q_{2l} is the $2l$th Legendre polynomial of the second kind. The

boundary conditions are

$$X(0) = 1, \tag{B2a}$$

$$X(+\infty) = 0. \tag{B2b}$$

As $Q_{2l}(0) = 0$, by Eq. (B2a) we have $c_1 = 1/P_{2l}(0)$. By Eq. (12.216) in Ref. [43], we also have

$$Q_{2l}(z) = \frac{P_{2l}(z)}{2} \ln \frac{1+z}{1-z} + R_{2l-1}(z), \tag{B3}$$

where R_{2l-1} is a polynomial of degree $(2l-1)$ with only odd-order terms; thus

$$X_l(\xi) = \frac{P_{2l}(j\xi)}{P_{2l}(0)} + c_2 \left(jP_{2l}(j\xi) \arctan \xi + R_{2l-1}(j\xi)\right) \tag{B4a}$$

$$= \left(\frac{1}{P_{2l}(0)} + jc_2 \arctan \xi\right) P_{2l}(j\xi) + c_2 R_{2l-1}(j\xi). \tag{B4b}$$

Using Eq. (B2b), we conclude that

$$\lim_{\xi \to +\infty} \left(\frac{1}{P_{2l}(0)} + jc_2 \arctan \xi\right) = 0 \tag{B5}$$

and

$$c_2 = \frac{2j}{\pi P_{2l}(0)}. \tag{B6}$$

By Theorem 1 below, a solution satisfying Eq. (B2) exists and it must be of the form

$$X_l(\xi) = \frac{1}{P_{2l}(0)} \left(P_{2l}(j\xi) + \frac{2j}{\pi} Q_{2l}(j\xi)\right). \tag{B7}$$

Now, because $P'_{2l}(0) = 0$, it follows that

$$X_l'(0) = \frac{2j}{\pi P_{2l}(0)} \frac{d}{d\xi} Q_{2l}(j\xi)\Big|_{\xi=0} \tag{B8a}$$

$$= -\frac{2}{\pi P_{2l}(0)} Q'_{2l}(0) \tag{B8b}$$

$$= -\frac{2}{\pi} \frac{1}{\frac{(-1)^l(2l-1)!!}{(2l)!!}} \frac{(-1)^l(2l)!!}{(2l-1)!!} \tag{B8c}$$

$$= -\frac{2}{\pi} \left[\frac{(2l)!!}{(2l-1)!!}\right]^2. \tag{B8d}$$

Theorem 1: A monotonically decreasing solution to Eq. (49) satisfying the boundary conditions (B2) exists.

Proof. When $l = 0$, $X_l(\xi) = 1 - (2/\pi) \arctan \xi$ is a valid solution, so we assume that $l \geq 1$.

Let X_n be a sequence of solutions to Eq. (49), defined on $0 \leq \xi \leq n$, with the boundary conditions

$$X_n(0) = 1, \tag{B9a}$$

$$X_n(n) = 0. \tag{B9b}$$

Choosing $c_1 = 1/P_{2l}(0)$ and $c_2 = -P_{2l}(in)/Q_{2l}(in)$ gives an explicit form for X_n.

We claim that X_n monotonically decreases in $(0, n)$ and prove this by contradiction.

Indeed, Eq. (49) gives

$$(1+\xi^2)X''(\xi) + 2\xi X'(\xi) = 2l(l+1)X(\xi). \tag{B10}$$

If X_n is not monotonic, there exists a local extremum $\xi_0 \in (0, n)$ such that $X_n'(\xi_0) = 0$. We see from Eq. (B10) that $X_n''(\xi_0)$ has the same sign as $X_n(\xi)$. Thus, if $X_n(\xi_0) > 0$, then ξ_0 is a local minimum. Therefore, there exists a local maximum $\xi_1 \in (\xi_0, n)$ such that $X_n(\xi_1) > 0$. However, at ξ_1, which is also an extremum, $X_n''(\xi_1)$ and $X_n(\xi)$ have different signs, which is a contradiction. Similarly, assuming that $X_n(\xi_0) < 0$ leads to a contradiction as well. Therefore, X_n monotonically decreases in $(0, n)$.

We also claim that $X_n(\xi)$ is increasing in n; that is, if $m > n$, then $X_m(\xi) \geq X_n(\xi)$ for $0 \leq \xi \leq n$. Indeed, monotonicity of $X_m(\xi)$ in ξ implies that $X_m(n) > 0$; thus $Z = X_m(\xi) - X_n(\xi)$ satisfies Eq. (49) with $Z(0) = 0$ and $Z(n) > 0$. By the same argument, Z cannot attain a negative minimum; thus $Z(\xi) > 0$ for all $0 < \xi < n$. Therefore, the limit

$$X_l = \lim_{n \to +\infty} X_n, \tag{B11}$$

exists and $X_l \geq 0$ is monotonically decreasing. We claim that

$$\lim_{\xi \to +\infty} X_l(\xi) = 0 \tag{B12}$$

and prove this by contradiction.

Assume that there exists $\epsilon > 0$ such that $X_l(\xi) \geq \epsilon$ for all $\xi \geq 0$. The integral of the left side of Eq. (49) yields

$$\int_0^t \left[(1+\xi^2)X_l'\right]' d\xi = (1+t^2)X_l'(t) - X_l'(0) \leq -X_l'(0). \tag{B13}$$

The integral of the right side of Eq. (49) yields

$$\int_0^t 2l(l+1)X_l(\xi)d\xi \geq 2l(l+1)\epsilon t. \tag{B14}$$

As $t \to +\infty$, we have $2l(l+1)\epsilon t > -X_l'(0)$, which is a contradiction, and Eq. (B12) follows.

[1] A. J. Bard and L. R. Faulkner, *Electrochemical Methods: Fundamentals and Applications* (John Wiley & Sons, Hoboken, New Jersey, 2001), 2nd ed.

[2] J. Newman and K. E. Thomas-Alyea, *Electrochemical Systems* (John Wiley & Sons, Hoboken, New Jersey, 2004).

[3] J. C. Myland and K. B. Oldham, How does the double layer at a disk electrode charge?, J. Electroanal. Chem. **575**, 81 (2005).

[4] M. Bleda-Martínez, J. Maciá-Agulló, D. Lozano-Castelló, E. Morallón, D. Cazorla-Amorós, and A. Linares-Solano, Role of surface chemistry on electric double layer capacitance of carbon materials, Carbon **43**, 2677 (2005).

[5] T. Pajkossy and D. Kolb, Double layer capacitance of Pt(111) single crystal electrodes, Electrochim. Acta **46**, 3063 (2001).

[6] T. R. Gore, T. Bond, W. Zhang, R. W. Scott, and I. J. Burgess, Hysteresis in the measurement of double-layer capacitance at the gold–ionic liquid interface, Electrochem. Commun. **12**, 1340 (2010).

[7] W. Sugimoto, T. Kizaki, K. Yokoshima, Y. Murakami, and Y. Takasu, Evaluation of the pseudocapacitance in RuO_2 with a RuO_2/GC thin film electrode, Electrochim. Acta **49**, 313 (2004).

[8] J. M. Soon and K. P. Loh, Electrochemical double-layer capacitance of MoS_2 nanowall films, Electrochem. Solid-State Lett. **10**, A250 (2007).

[9] A. A. F. Grupioni, E. Arashiro, and T. A. F. Lassali, Voltammetric characterization of an iridium oxide-based system: The pseudocapacitive nature of the $Ir_{0.3}Mn_{0.7}O_2$ electrode, Electrochim. Acta **48**, 407 (2002).

[10] M. S. Halper and J. C. Ellenbogen, *Supercapacitors: A Brief Overview* (The MITRE Corporation, McLean, Virginia, USA, 2006), Vol. 1.

[11] J. Newman, Resistance for flow of current to a disk, J. Electrochem. Soc. **113**, 501 (1966).

[12] J. Newman, Current distribution on a rotating disk below the limiting current, J. Electrochem. Soc. **113**, 1235 (1966).

[13] A. C. West and J. Newman, Current distribution near an electrode edge as a primary distribution is approached, J. Electrochem. Soc. **136**, 2935 (1989).

[14] W. J. Albery, M. L. Hitchman, and W. J. Albery, *Ring-Disc Electrodes* (Clarendon Press Oxford, Oxford, UK, 1971).

[15] J. C. Weaver and Y. A. Chizmadzhev, Theory of electroporation: A review, Bioelectrochem. Bioenerg. **41**, 135 (1996).

[16] A. Lasia, in *Modern Aspects of Electrochemistry* (Springer, New York, 2002), p. 143.

[17] D. Boinagrov, X. Lei, G. Goetz, T. I. Kamins, K. Mathieson, L. Galambos, J. S. Harris, and D. Palanker, Photovoltaic pixels for neural stimulation: Circuit models and performance, IEEE Trans. Biomed. Circuits Syst. **10**, 85 (2015).

[18] K. Nisancioğlu and J. Newman, The transient response of a disk electrode with controlled potential, J. Electrochem. Soc. **120**, 1356 (1973).

[19] K. Nisancioğlu and J. Newman, The transient response of a disk electrode, J. Electrochem. Soc. **120**, 1339 (1973).

[20] J. Newman, Frequency dispersion in capacity measurements at a disk electrode, J. Electrochem. Soc. **117**, 198 (1970).

[21] M. R. Behrend, A. K. Ahuja, and J. D. Weiland, Dynamic current density of the disk electrode double-layer, IEEE Trans. Biomed. Eng. **55**, 1056 (2008).

[22] D. R. Cantrell, S. Inayat, A. Taflove, R. S. Ruoff, and J. B. Troy, Incorporation of the electrode-electrolyte interface into finite-element models of metal microelectrodes, J. Neural Eng. **5**, 54 (2007).

[23] J. C. Myland and K. B. Oldham, The excess current in cyclic voltammetry arising from the presence of an electrode edge, J. Solid State Electrochem. **18**, 3259 (2014).

[24] L. Bieniasz, Theory of potential step chronoamperometry at a microband electrode: Complete explicit semi-analytical formulae for the faradaic current density and the faradaic current, Electrochim. Acta **178**, 25 (2015).

[25] A. Sue, P. Wong, P. Tran, Q. Li, and P. Carter, in *2015 7th International IEEE/EMBS Conference on Neural Engineering (NER)* (IEEE, Montpellier, France, 2015), p. 490.

[26] B. Conway and W. Pell, Double-layer and pseudocapacitance types of electrochemical capacitors and their applications to the development of hybrid devices, J. Solid State Electrochem. **7**, 637 (2003).

[27] E. Barsoukov and J. R. Macdonald, *Impedance Spectroscopy: Theory, Experiment, and Applications* (John Wiley & Sons, Hoboken, New Jersey, 2005).

[28] B. Wang, Ph.D. thesis, Viterbi School of Engineering, University of Southern California, 2016.

[29] K. B. Oldham, The *RC* time "constant" at a disk electrode, Electrochem. Commun. **6**, 210 (2004).

[30] O. Ciftja and I. Hysi, The electrostatic potential of a uniformly charged disk as the source of novel mathematical identities, Appl. Math. Lett. **24**, 1919 (2011).

[31] See the Supplemental Material at http://link.aps.org/supplemental/10.1103/PhysRevApplied.13.014004 for a video showing the dynamics of the current and potential distribution on a disk electrode in electrolyte.

[32] S. F. Cogan, J. Ehrlich, T. D. Plante, A. Smirnov, D. B. Shire, M. Gingerich, and J. F. Rizzo, Sputtered iridium oxide films for neural stimulation electrodes, J. Biomed. Mater. Res. Part B: Appl. Biomater. **89**, 353 (2009).

[33] T. Pauporté, D. Aberdam, J.-L. Hazemann, R. Faure, and R. Durand, X-ray absorption in relation to valency of iridium in sputtered iridium oxide films, J. Electroanal. Chem. **465**, 88 (1999).

[34] S. F. Cogan, Neural stimulation and recording electrodes, Annu. Rev. Biomed. Eng. **10**, 275 (2008).

[35] J. Duru, Master's thesis, ETH Zürich, 2019.

[36] B. A. Troesch and R. Troesch, A remark on the sloshing frequencies for a half-space, Zeitschrift für angewandte Mathematik und Physik ZAMP **23**, 703 (1972).

[37] T. Flores, G. Goetz, X. Lei, and D. Palanker, Optimization of return electrodes in neurostimulating arrays, J. Neural Eng. **13**, 036010 (2016).

[38] T. Flores, X. Lei, T. Huang, H. Lorach, R. Dalal, L. Galambos, T. Kamins, K. Mathieson, and D. Palanker, Optimization of pillar electrodes in subretinal prosthesis for enhanced proximity to target neurons, J. Neural Eng. **15**, 036011 (2018).

[39] T. Flores, T. W. Huang, H. Lorach, R. Dalal, X. Lei, T. Kamins, K. Mathieson, and D. V. Palanker, Vertical walls surrounding pixels in subretinal space reduce stimulation

threshold and improve contrast, Invest. Ophthalmol. Vis. Sci. **59**, 3975 (2018).

[40] E. Ho, H. Lorach, T. W. Huang, X. Lei, T. Flores, T. Kamins, L. Galambos, K. Mathieson, and D. V. Palanker, Grating acuity of prosthetic vision in blind rats matches the pixel pitch of photovoltaic subretinal arrays below 50 μm, Invest. Ophthalmol. Vis. Sci. **59**, 3977 (2018).

[41] E. Musk *et al.*, An integrated brain-machine interface platform with thousands of channels, BioRxiv, 703801 (2019).

[42] B. Wang, A. Petrossians, and J. D. Weiland, Reduction of edge effect on disk electrodes by optimized current waveform, IEEE Trans. Biomed. Eng. **61**, 2254 (2014).

[43] G. B. Arfken and H. Weber, *Mathematical Methods for Physicists* (Elsevier, Burlington, MA, 2005).